Synthesis, optical characterization, and simulation of organo-metal halide perovskite materials

Abdy, Hamed; Aletayeb, Arash; Bashirpour, Mohammad; Heydari, Zahra; Kolahdouz, Mohammadreza; Asl-Soleimani, Ebrahim; Kolahdouz, Zahra ; Zhang, Guoqi

DOI
10.1016/j.ijleo.2019.06.007

Publication date
2019

Document Version
Final published version

Published in
Optik

Citation (APA)
Abdy, H., Aletayeb, A., Bashirpour, M., Heydari, Z., Kolahdouz, M., Asl-Soleimani, E., Kolahdouz, Z., & Zhang, G. (2019). Synthesis, optical characterization, and simulation of organo-metal halide perovskite materials. *Optik*, *191*, 100-108. https://doi.org/10.1016/j.ijleo.2019.06.007

Optik - International Journal for Light and Electron Optics 191 (2019) 100–108

Contents lists available at ScienceDirect

Optik

journal homepage: www.elsevier.com/locate/ijleo

Original research article

Synthesis, optical characterization, and simulation of organo-metal halide perovskite materials

Hamed Abdy[a], Arash Aletayeb[a], Mohammad Bashirpour[a], Zahra Heydari[a], Mohammadreza Kolahdouz[a,*], Ebrahim Asl-Soleimani[a], Zahra Kolahdouz[b,*], Guoqi Zhang[b]

[a] Department of Electrical and Computer Engineering, University of Tehran, Tehran, Islamic Republic of Iran
[b] Delft Institute of Microsystems and Nanoelectronics (DIMES-EKL), Delft University of Technology, Delft, the Netherlands

ARTICLE INFO

Keywords:
Finite differential time domain
Optical characterization
Organo-metal halide perovskite
Simulation
Two-step deposition
Methylammonium lead iodide

ABSTRACT

In recent years, the significant progress of organic-inorganic hybrid perovskite solar cells has surprised the photovoltaic community. Moreover, many other optoelectronic devices have been fabricated using this new generation of materials which makes it more attractive for researchers. Among different physical and chemical synthesis methods, we have taken on a two-step solution-based synthesis procedure to deposit $CH_3NH_3PbI_3$ with 1.55 eV energy band gap in ambient air condition. Various optoelectrical characterization tools have been used to thoroughly investigate the perovskite film quality. Simulations were carried out using Finite-Difference Time-Domain method (FDTD) for studying light absorption mechanism in perovskite films. Various surface roughness amounts were applied to the simulations to achieve a good consistency between experimental and theoretical absorption curves. This approach can give an insight into how surface roughness effectively impacts on the optical characteristics of the synthesized layer. Moreover, light absorption mechanism has been also investigated which demonstrates how light with a wavelength of more than 540 nm can be transmitted from a 400 nm thick perovskite layer. Simulations also illustrate how surface roughness can help light trapping in the perovskite layer.

1. Introduction

Nowadays, scientists have discovered many new generations of optical materials and their constructions for different optical applications [1–5]. One of these exciting novel substances is a branch of perovskite materials with photoconductive properties which has surpassed other materials in the field of optoelectronics based on its applications [6]. The crystal structure of these semiconductor perovskites (called perovskites in the rest of this paper) is in the form of ABX_3 in which A represents methylammonium (CH_3NH_3), formamidinium ($CH_2(NH_2)_2$) or cesium (Cs); B can be replaced with lead (Pb) or tin (Sn) and finally halide atoms like Cl, Br and I can be substituted with the X symbol [7]. In summary, the main reasons for the superiority of perovskite are its remarkable advantages such as having a direct band gap and good absorption properties, low-cost synthesis methods, high charge carrier mobility, low exciton binding energy, long carrier diffusion length and most importantly the tunability of the band gap [8,9].

Thus, these useful properties, have made the power conversion efficiency (PCE) of the perovskite solar cells reach above 23% [10]. In addition to energy harvesting, different compounds of this material has been used to fabricate other devices such as the light

* Corresponding authors.
E-mail addresses: kolahdouz@ut.ac.ir (M. Kolahdouz), Z.KolahdouzEsfahani@tudelft.nl (Z. Kolahdouz).

https://doi.org/10.1016/j.ijleo.2019.06.007
Received 18 December 2018; Received in revised form 1 June 2019; Accepted 3 June 2019

emitting diodes (LEDs) [11], low power lasing in various colors and different wavelengths [12], visible and x-ray photodetectors [13], optical sensors [14], field effect transistors [15], and Schottky diodes [16].

In order to have an optoelectronic device with a desired functionality, optimization of the material synthesis approach is of great importance [17]. Generally, some chemical synthesis methods based on solution approaches such as solvent-engineering [18,19], solvent-solvent extraction [20], one-step [21] and two-step [22], have been introduced along with physical methods such as thermal evaporation [23,24] of the organo-metal trihalide perovskite material. It must be mentioned that in this work, we have used the two-step solution deposition method to synthesize $CH_3NH_3PbI_3$ or $MAPbI_3$ perovskite materials. In the first step of this method, PbI_2 in DMF solution was used to deposit a PbI_2 layer. The next step was converting this layer into perovskite by spin coating of MAI in isopropanol (IPA) solution on it.

Fast crystallization of dissolved PbI_2 in DMF, results in different crystal sizes in the final perovskite layer. It has been also learned that applying different concentrations of dissolved MAI powder in isopropanol (IPA), changes the crystal size of $MAPbI_3$. In fact, by changing the MAI/IPA solution concentration from 0.063 M to 0.038 M, the average crystal size of $MAPbI_3$ increases from 90 nm to 700 nm [25]. An important consequence of increasing the crystal size is the photocurrent density raise [26]. It is obvious that the larger the crystals of the $MAPbI_3$, the higher the short-circuit current which is due to higher light absorption and better dissociation of electron-hole pairs [27–29]. To be more precise, current density increasing in large perovskite crystals is due to the reduced number of dangling bonds in the interfacial area in addition to the formation of bigger crystal grains, which result in an impressive reduction of the electron – holes recombination in the trap states of the material [30]. Also, another advantage of $MAPbI_3$ large crystal grains is the reduction of bulk defects which causes higher charge mobility and better carrier propagation to reach the cell electrodes [31].

One of the important utilized characterizations for checking crystallinity of $MAPbI_3$ is X-Ray Diffraction (XRD) which shows the formation of different $MAPbI_3$ crystal planes [27,32]. It has been found that the XRD pattern of perovskite material before the annealing step is a bit different from the final $MAPbI_3$ layer [18,33]. Jeon et al. declared that the peaks below 10° for the perovskite material before the annealing step are due to the existence of solvent materials [18].

Maximizing the light absorption of the $MAPbI_3$ material is obviously vital for solar application [34,35]. Diffuse Reflectance Spectroscopy (DRS) equipment can be used to calculate the optical band gap. By extracting the starting absorbance wavelength (λ) of the material and using the following equation:

$$E = \frac{h.\,c}{\lambda} \tag{1}$$

where E represents the energy band gap of the material, h is the plank constant, c is the light velocity, and λ denotes the wavelength related to the band gap emission of the material [36,37].

Another important factor in solar cells which can affect light absorption is the surface roughness [38]. In this work, the root-mean-square (rms) value, R_q, has been used for surface roughness evaluation as follows:

$$R_q = \text{rms} = \sqrt{\frac{\sum_{i=1}^{n} y_i^2}{n}} \tag{2}$$

where y_i is a vertical distance from the center line of the surface curve, and n is the total number of vertical measurements taken within a specific cutoff distance [39]. The rest of this paper starts with describing our experimental method in the Materials and Methods section, then the Simulation Method section explains the simulation procedure. The Results and Discussion section represents our results and discusses mainly the reasons. Finally, the Conclusions section draws our conclusions.

2. Materials and methods

In this study, the two-step solution deposition method has been used for perovskite synthesis. After optimizing the synthesis method, characterization of the perovskite material has been carried out. The surface coverage and the morphology of the perovskite layers were analyzed by field emission scanning electron microscopes (FESEM images). In order to thoroughly understand the physical and optical behaviors of the material, the synthesized perovskite material was analyzed using X-Ray Diffraction, photoluminescence, and DRS. While perovskite surface roughness can play an important role in its light absorption behavior, Finite-Difference Time-Domain method (FDTD) has been used to simulate the perovskite on FTO for finding a physical insight about light absorption in our experiments. FDTD is designed based on Maxwell's electromagnetic wave equations to acquire precise optical responses [40]. Surface roughness has been introduced into the simulation to reproduce the experimental results.

In this section, our experimental and simulation methods are explained in more details.

2.1. Synthesis of MAI

For the preparation of CH_3NH_3I powder, methylamine (27.86 ml, 40% in methanol), and hydroiodic acid (30 ml, 57 wt% in water) were mixed at 0 °C and stirred for 4 h. Next, the precipitate was recovered by thermal evaporation at 55 °C for 1 h. Thereafter, the product was dissolved in ethanol and then washed with diethyl ether. Finally, the solution was dried in a vacuum oven for 24 h at 60 °C, to evaporate the solvents while forming the white MAI powder as a result.

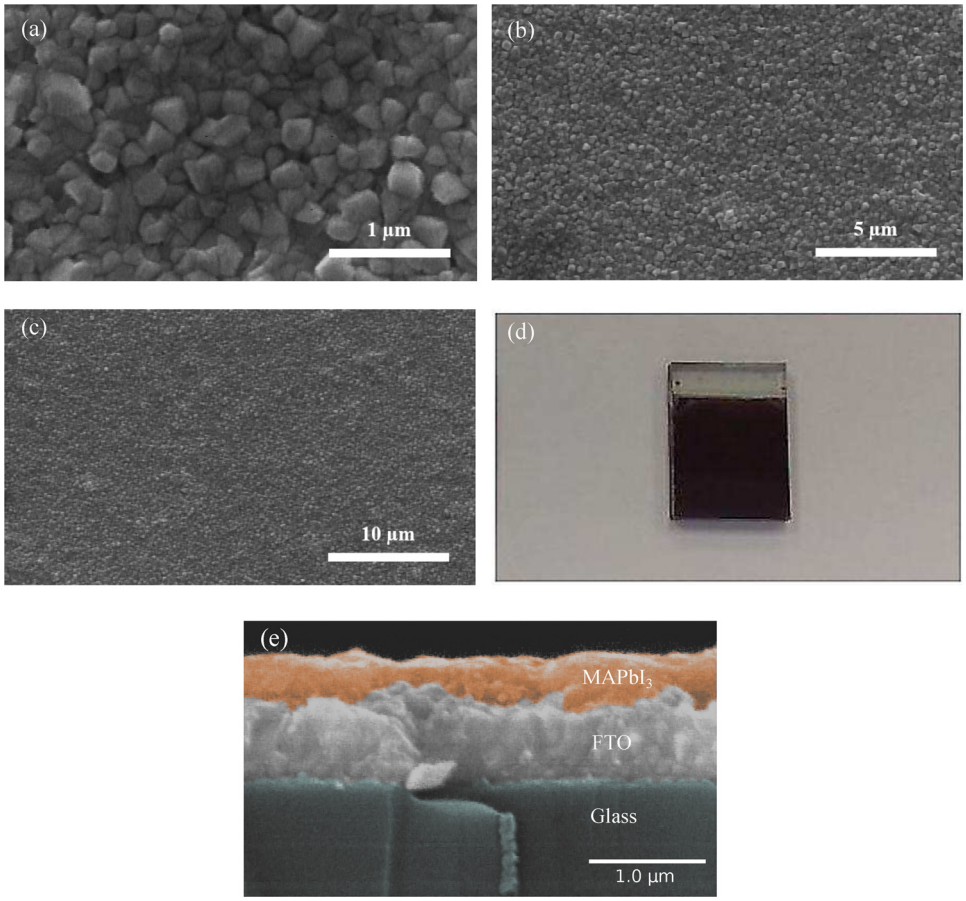

Fig. 1. a, b, c) FESEM top view images of the $MAPbI_3$, d) Optical image of the $MAPbI_3$ perovskite layer on the FTO substrate, and e) FESEM cross view image of the synthesized $MAPbI_3$ layer.

2.2. Deposition of $MAPbI_3$ perovskite material

As mentioned earlier, the two-step synthesis method was applied to form the perovskite layer in this work. But before spin coating, the FTO (Fluorine doped tin oxide) substrate was cleaned in the ultrasonic bath containing DI water, methanol, ethanol, and isopropanol, soaking in each for 10 min subsequently [41].

After FTO cleaning, the $MAPbI_3$ perovskite layer was formed according to the following steps. First, the 1 M PbI_2 solution was prepared by dissolving 462 mg PbI_2 (99%) in 1 ml N, N-dimethylformamide (DMF, 99.8%) through stirring at 70 °C. This solution was spin coated on the substrate at 3000 rpm. for 5 s and 5000 rpm for 5 s. Next, the film was dried at 40 °C for 3 min and 100 °C for 5 min. Afterward, the film was cooled at room temperature for at least 10 min.

For step two, 0.050 M (8 mg ml^{-1}) CH_3NH_3I solution in 2-propanol was prepared under stirring at room temperature. Then, 200 µl of this solution was loaded on the PbI_2-coated substrate (1 min loading time) and later was spun at 4000 rpm. for 20 s. Finally, in order to form the $MAPbI_3$ dried layer, the film was annealed at 100 °C for 5 min [42].

2.3. Simulation method

In this study, the FDTD method has been used to simulate the perovskite layer deposited on FTO. The $MAPbI_3$ and FTO thickness was 400 nm and 1 µm respectively, based on the experimental data extracted from FESEM pictures (see Fig. 1). The incident light propagated as a plane wave with the visible wavelengths ranging from 400 nm to 820 nm, into the Z-direction downwards. The boundary conditions were set to the perfectly matched layers (PMLs), both symmetrical and asymmetrical, in the Z-direction, X-direction, and Y-direction, respectively. Also, the several frequency-domain transmission monitors have been used at the top of the simulation region, parallel to the perovskite material in order to capture the normalized absorption, transmission and reflection spectra [43].

Triangle is the closest simple shape to the surface roughness of the experimentally deposited perovskite film, so it has been implemented to simulate the surface roughness. According to the average grain size in experimentally deposited perovskite films, the base of the simulated triangles set to 200 nm (see the shape and size of these grains in Fig. 1 a). Various surface roughness heights

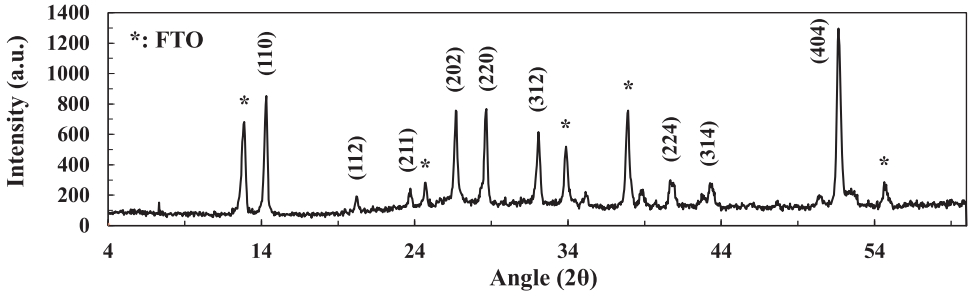

Fig. 2. XRD pattern for MAPbI3 perovskite material spin-coated on FTO substrate. The crystalline plane peaks for $MAPbI_3$ perovskite material are (110), (112), (211), (202), (220), (312), (224), (314), (404) at the angles of 14.3°, 20.2°, 24.7°, 26.6°, 28.6°, 31.2°, 40.9°, 43.3°, 51.6° respectively.

have been used to find the best results matching the experiments.

An important concept of the FDTD simulation method is that all calculations used for solving Maxwell's equations are based on the relative permittivity constant (ε) of the material. So, in order to introduce the $MAPbI_3$ perovskite material in the simulation, both the refractive index (n) and the extinction coefficient (k) which are related to epsilon (ε) were used from the previous reports [43,44]. It must be noted that these parameters have been employed according to the range of the visible wavelengths in our experimental characterizations.

3. Results and discussion

One of the most important characterizations for all perovskite materials in optoelectronic devices is through FESEM images of the surface covering. Fig. 1 represents the FESEM and optical images of the $MAPbI_3$ layer produced trough two-step synthesis method. These images illustrate the perovskite crystals and the grain boundaries, also showing the good surface coating of the synthesized layer. It is remarkable that our synthesized perovskite material was spin-coated in the ambient air condition. Nevertheless, we have succeeded in having an even, pinhole-free perovskite layer with an average grain size of 200 nm without using a glovebox. The shape of these grains, as can be seen in Fig. 1a, is approximately a cube whose half is diagonally buried in the bulk and as a result, it has been concluded that the best 2D shape for implementing the roughness into the simulation, is the triangle with a base size equal to the average grain size, i.e. 200 nm.

As can be seen in Fig. 2, the XRD pattern and crystalline planes for dried perovskite layers are completely matching to $MAPbI_3$ without DMF peaks which indicates the evaporation of the solvent after the annealing process, resulting to a solvent-free perovskite film with good crystallinity. Furthermore, the crystalline plane peaks for $MAPbI_3$ perovskite material are (110), (112), (211), (202), (220), (312), (224), (314), (404) at the angles of 14.3°, 20.2°, 24.7°, 26.6°, 28.6°, 31.2°, 40.9°, 43.3°, 51.6° respectively.

The amount of light absorption, transmission, and reflection of the $MAPbI_3$ perovskite material was measured in the range of

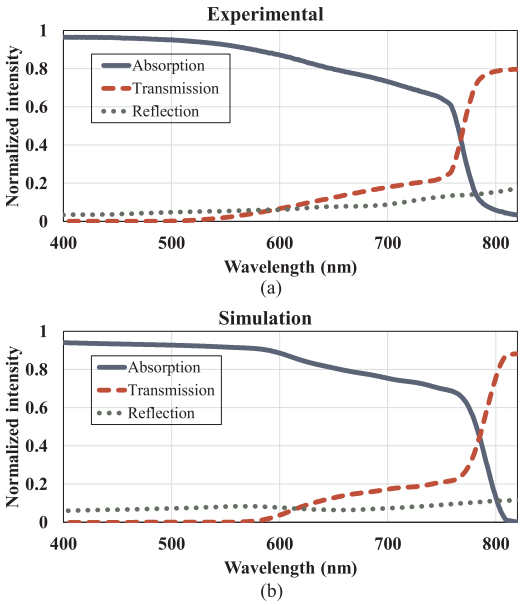

Fig. 3. The normalized absorption, reflection, and transmission spectra of $MAPbI_3$ perovskite material obtained by (a) experiment and (b) simulation (surface roughness with rms of 37.53 nm). These results show good agreement between theory and experiment.

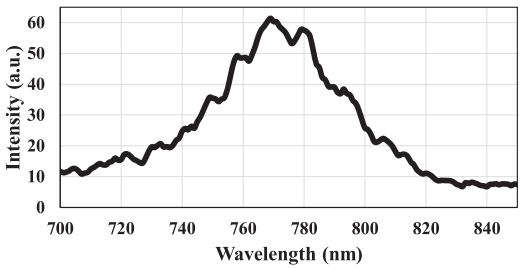

Fig. 4. Normalized photoluminescence spectrum of $MAPbI_3$ perovskite material. The peak at the wavelength of 771 nm relates to the energy band gap of $MAPbI_3$.

400–820 nm (see Fig. 3). As expected, the $MAPbI_3$ light absorption begins at 800 nm, linked to its energy band gap. By considering Eq. (1) and 778 nm as the starting absorbance wavelength (λ) of the $MAPbI_3$, 1.59 eV band gap was obtained for the synthesized perovskite material.

For photoluminescence (PL) characterization, the synthesized $MAPbI_3$ by a two-step spin coating method was excited with a LASER source at a wavelength of 550 nm. As can be seen in Fig. 4, PL emission was observed between 740 nm and 800 nm which is an extra confirmation for the calculated band-gap.

The $MAPbI_3$ perovskite layer was simulated by FDTD simulation method. For intended optical simulation by FDTD, the refractive index and extinction coefficient of material are required as the two main parameters. So, by inserting perovskite's n and k optical parameters, and various surface roughness heights, $MAPbI_3$'s absorption, transmission, and reflection spectra were extracted using the experimental conditions in the wavelength range of 400–820 nm. The following equation was used for finding the distance between the experimental and simulation curves:

$$D = \sum_{n=400nm}^{n=820nm} (|i^{A}_{Exp.}(n) - i^{A}_{Sim.}(n)| + |i^{T}_{Exp.}(n) - i^{T}_{Sim.}(n)| + |i^{R}_{Exp.}(n) - i^{R}_{Sim.}(n)|) \quad (3)$$

where D is the distance between two sets (absorption, transmission, and reflection) of simulation and experimental curves, n is the wavelength of the incident light, and i is the intensity of absorbed (A), transmitted (T), and reflected (R) light with *Exp.* and *Sim.* indicating experimental and simulation results, respectively. Table 1 represents the results obtained using Eq. (3).

As can be seen in Table 1 and Fig. 5, the best match between the experimental and simulation curves is related to the rms roughness of 37.53 nm. This amount gives us an insight into the roughness of the experimentally deposited perovskite layer. Fig. 5 also reveals the effect of surface roughness on light trapping. It shows an increment in absorption and decrement in reflection by increasing the surface roughness. This figure shows, surface roughness does not affect transmission significantly. Hence it can be concluded that surface roughness increment increases light trapping which can help more efficient light absorption in the perovskite layer. Fig. 3 shows the experimental data and obtained simulation results for rms roughness of 37.53 nm. There is a slight difference between the simulation and experimental curves. The backside roughness, which decreases the back reflection, has not been considered in the simulation. It should be noted that, as mentioned earlier, a wavelength-dependent complex refractive index has been taken into account in simulation conditions which can be another source of variation in the experimental and simulation results. It

Table 1
D values obtained from Eq. (3) for various roughness values. The simulated device with the roughness of 37.53 nm shows the minimum D value, indicating the best match between the experimental and simulation curves.

Roughness (nm)	D
5.77	149.35
8.66	144.62
11.55	135.50
14.43	125.98
17.32	114.89
20.21	102.78
23.09	90.41
25.98	77.25
28.87	64.85
31.75	54.20
34.64	42.66
37.53	**40.49**
40.41	40.86
43.30	41.82

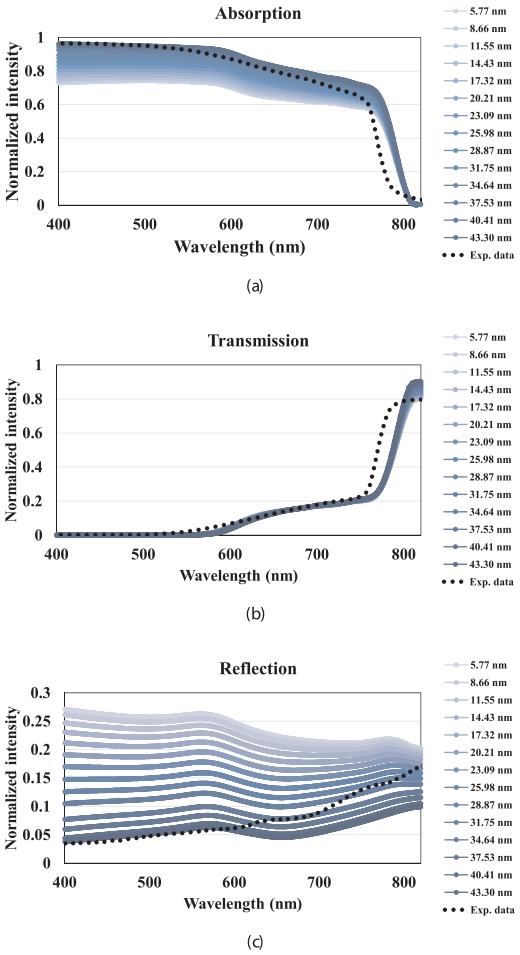

Fig. 5. (a) Absorption, (b) transmission, and (c) reflection spectra extracted for various amounts of surface roughness using FDTD simulation. The dotted lines show experimental data.

also shows that the transmission starts to increase in wavelengths between 500 nm and 600 nm. To study this phenomenon more precisely, the penetration depth of light in the perovskite layer was extracted from the simulation for different wavelengths. From Fig. 6, which represented the light penetration depth in perovskite against the wavelength of the light, it can be seen that a perovskite layer with a depth of less than 150 nm can absorb light waves below 500 nm. For the wavelengths above 500 nm, an intense increment of the penetration depth can be seen. The light waves above 540 nm can't be absorbed completely in the perovskite layer, hence gives an increment to the transmission amount.

Photocurrent simulation and extracting electric field distribution can help us investigate the light absorption mechanism more deeply [5]. Fig. 7 represents electric field distribution in the perovskite film for 5 different wavelengths from 400 nm to 800 nm. It also shows the effect of surface roughness on the electric field distribution. Reaching $|E/E_0|$ to 0 at the bottom of the perovskite layer only at the wavelengths of 400 nm and 500 nm is another verification to our discussion about the light penetration depth in

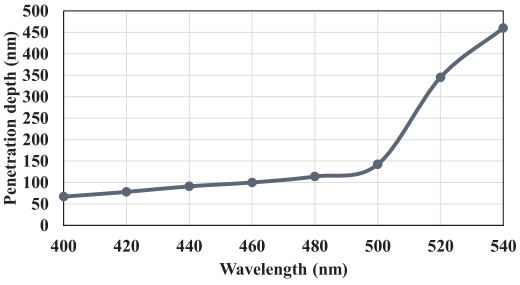

Fig. 6. Light penetration depth in perovskite against the light wavelength.

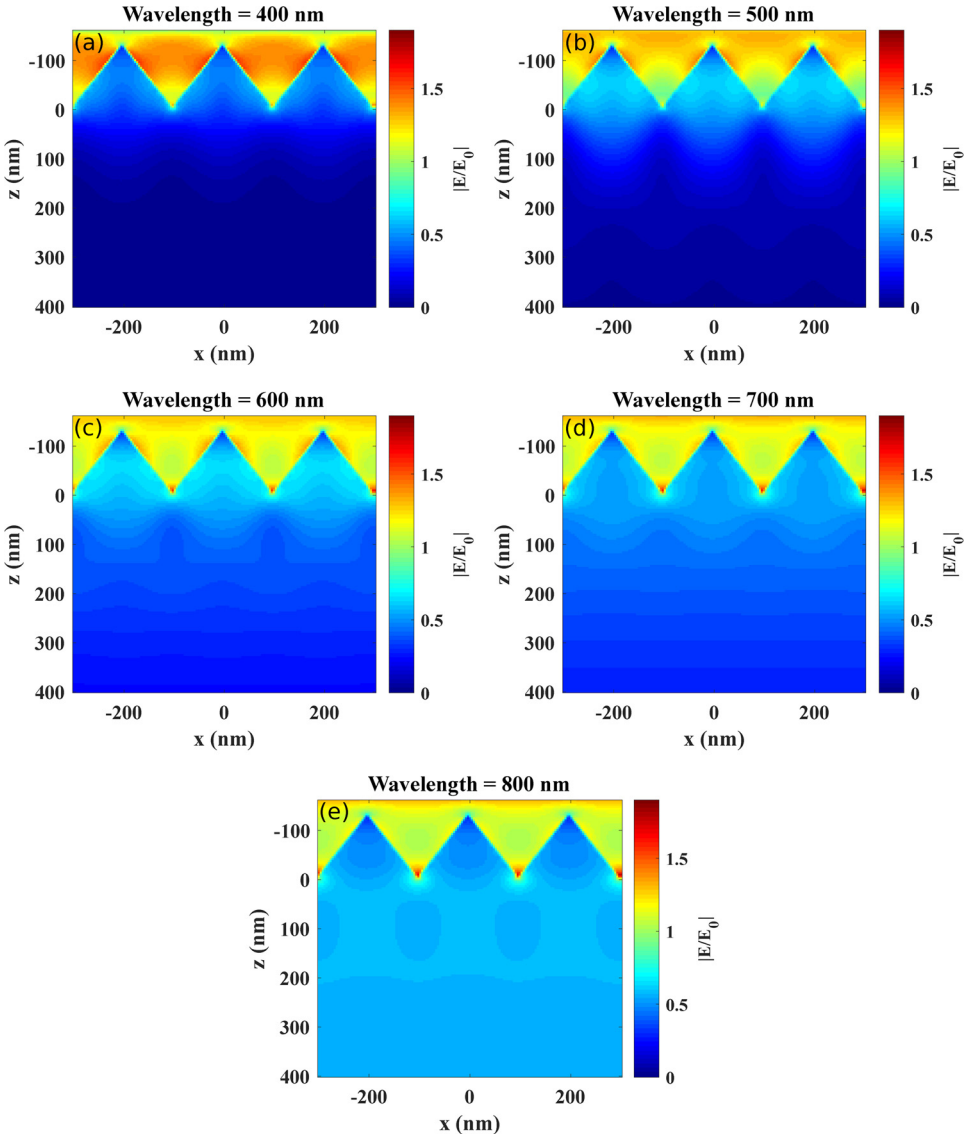

Fig. 7. Electric field distribution in the simulated perovskite film for 5 different wavelengths of (a) 400 nm, (b) 500 nm, (c) 600 nm, (d) 700 nm, and (e) 800 nm.

perovskite. Another interesting phenomenon is how surface roughness affects electric field distribution in the perovskite layer. This surface roughness can help to change the light distribution in the perovskite layer and improve light absorption. However, it is worth noting here that surface roughness can, on the other hand, degrade the performance of the cells by increasing the amount of surface traps. A tradeoff between light absorption and amount of surface traps should be reached for the best solar cell performance.

4. Conclusions

In summary, the two-step synthesis method was applied to produce the $MAPbI_3$ perovskite layer in ambient air condition without using a glovebox in different physical and chemical perovskite synthesis methods. Several important optical characterizations were used to thoroughly understand the physical behavior of the perovskite material. The quality of our synthesized material was approved by the XRD measurements and SEM images, showing the quality of the surface coverage and the perovskite morphology. Also, the $MAPbI_3$ energy band gap, absorption, transmission, and reflection spectrums were measured by PL and DRS characterizations. The FDTD optical simulation method was employed to investigate light absorption mechanisms in the perovskite layer with various amounts of surface roughness. The experimental and theoretical curves of the perovskite material show a good consistency for the surface roughness with rms of 37.53 nm. Simulations show that lights having the wavelength of more than 540 nm can partially transmit from the perovskite layer with a thickness of 400 nm. Surface roughness may cause light trapping in the deposited film,

however, a good tradeoff between the increment of surface traps and light trapping should be achieved for the best solar cell performance.

Conflict of interest

The authors declare that they have no conflict of interest.

References

[1] H.H. Radamson, M. Kolahdouz, S. Shayestehaminzadeh, A.A. Farniya, S. Wissmar, Carbon-doped single-crystalline SiGe/Si thermistor with high temperature coefficient of resistance and low noise level, Appl. Phys. Lett. 97 (2010) 223507, , https://doi.org/10.1063/1.3524211.

[2] M. Kolahdouz, A.A. Farniya, L. Di Benedetto, H.H. Radamson, Improvement of infrared detection using Ge quantum dots multilayer structure, Appl. Phys. Lett. 96 (2010), https://doi.org/10.1063/1.3441120.

[3] F. Karegar, M. Kolahdouz, F.D. Nayeri, R. Soleimanzedeh, M. Hosseini, Light emitting n-ZnO nanotube / n + -GaAs heterostructures processed at low temperatures, IEEE Opt. Technol. Lett. 1135 (2015) 10–13, https://doi.org/10.1109/LPT.2015.2424454.

[4] S. Ghorbani, M. Bashirpour, J. Poursafar, M. Kolahdouz, M. Neshat, A. Valinejad, Thin film tandem nanoplasmonic photoconductive antenna for high performance terahertz detection, Superlatt. Microstruct. 120 (2018), https://doi.org/10.1016/j.spmi.2018.06.029.

[5] M. Bashirpour, M. Forouzmehr, S.E. Hosseininejad, M. Kolahdouz, M. Neshat, Improvement of terahertz photoconductive antenna using optical antenna array of ZnO nanorods, Sci. Rep. 9 (2019) 1414, https://doi.org/10.1038/s41598-019-38820-3.

[6] C.A. Ubani, M.A. Ibrahim, M.A.M. Teridi, Moving into the domain of perovskite sensitized solar cell, Renew. Sustain. Energy Rev. 72 (2017) 907–915, https://doi.org/10.1016/j.rser.2017.01.025.

[7] M. Grätzel, The light and shade of perovskite solar cells, Nat. Mater. 13 (2014) 838–842, https://doi.org/10.1038/nmat4065.

[8] S. De Wolf, J. Holovsky, S.J. Moon, P. Löper, B. Niesen, M. Ledinsky, F.J. Haug, J.H. Yum, C. Ballif, Organometallic halide perovskites: sharp optical absorption edge and its relation to photovoltaic performance, J. Phys. Chem. Lett. 5 (2014) 1035–1039, https://doi.org/10.1021/jz500279b.

[9] C.C. Stoumpos, C.D. Malliakas, M.G. Kanatzidis, Semiconducting tin and lead iodide perovskites with organic cations: phase transitions, high mobilities, and near-infrared photoluminescent properties, Inorg. Chem. 52 (2013) 9019–9038, https://doi.org/10.1021/ic401215x.

[10] M.A. Green, Y. Hishikawa, E.D. Dunlop, D.H. Levi, J. Hohl-Ebinger, M. Yoshita, A.W.Y. Ho-Baillie, Solar cell efficiency tables (Version 53), Prog. Photovolt. Res. Appl. 27 (2019) 3–12, https://doi.org/10.1002/pip.3102.

[11] O.A. Jaramillo-Quintero, R.S. Sanchez, M. Rincon, I. Mora-Sero, Bright visible-infrared light emitting diodes based on hybrid halide perovskite with Spiro-OMeTAD as a hole-injecting layer, J. Phys. Chem. Lett. 6 (2015) 1883–1890, https://doi.org/10.1021/acs.jpclett.5b00732.

[12] F. Deschler, M. Price, S. Pathak, L.E. Klintberg, D.D. Jarausch, R. Higler, S. Hüttner, T. Leijtens, S.D. Stranks, H.J. Snaith, M. Atatüre, R.T. Phillips, R.H. Friend, High photoluminescence efficiency and optically pumped lasing in solution-processed mixed halide perovskite semiconductors, J. Phys. Chem. Lett. 5 (2014) 1421–1426, https://doi.org/10.1021/jz5005285.

[13] D.M. Panneerselvam, M.Z. Kabir, Evaluation of organic perovskite photoconductors for direct conversion X-ray imaging detectors, J. Mater. Sci. Mater. Electron. 28 (2017) 7083–7090, https://doi.org/10.1007/s10854-017-6409-5.

[14] H.-R. Xia, J. Li, W.-T. Sun, L. Peng, Organohalide lead perovskite based photodetectors with much enhanced performance, Chem. Commun. 50 (2014) 13695–13697, https://doi.org/10.1039/C4CC05960C.

[15] Y. Mei, C. Zhang, Z.V. Vardeny, O.D. Jurchescu, Electrostatic gating of hybrid halide perovskite field-effect transistors: balanced ambipolar transport at room-temperature, MRS Commun. 5 (2015) 297–301, https://doi.org/10.1557/mrc.2015.21.

[16] L. Chen, J. Deng, H. Gao, Q. Yang, G. Wang, L. Kong, M. Cui, Z. Zhang, Organometallic hybrid perovskites: structural, optical characteristic and application in Schottky diode, J. Mater. Sci. Mater. Electron. 27 (2016) 4275–4280, https://doi.org/10.1007/s10854-016-4293-z.

[17] S.A. Bretschneider, J. Weickert, J.A. Dorman, L. Schmidt-Mende, Research update: physical and electrical characteristics of lead halide perovskites for solar cell applications, APL Mater. 2 (2014) 040701, , https://doi.org/10.1063/1.4871795.

[18] N.J. Jeon, J.H. Noh, Y.C. Kim, W.S. Yang, S. Ryu, S. Il Seok, Solvent engineering for high-performance inorganic-organic hybrid perovskite solar cells, Nat. Mater. 13 (2014) 1–7, https://doi.org/10.1038/nmat4014.

[19] H. Abdy, A. Aletayeb, M. Kolahdouz, E.A. Soleimani, Investigation of metal-nickel oxide contacts used for perovskite solar cell, AIP Adv. 9 (2019) 15216.

[20] Y. Zhou, M. Yang, W. Wu, A.L. Vasiliev, K. Zhu, N.P. Padture, Room-temperature crystallization of hybrid-perovskite thin films via solvent-Solvent extraction for high-performance solar cells, J. Mater. Chem. A (2015) 1–6, https://doi.org/10.1039/C5TA00477B.

[21] B.-E. Cohen, L. Etgar, Parameters that control and influence the organo-metal halide perovskite crystallization and morphology, Front. Optoelectron. 9 (2016) 44–52, https://doi.org/10.1007/s12200-016-0630-3.

[22] M.R. Filip, C. Verdi, F. Giustino, GW band structures and carrier effective masses of CH3NH3PbI3 and hypothetical perovskites of the type APbI3: A = NH4, PH4, AsH4, and SbH4, J. Phys. Chem. C 119 (2015) 25209–25219, https://doi.org/10.1021/acs.jpcc.5b07891.

[23] S. Brittman, G.W.P. Adhyaksa, E.C. Garnett, The expanding world of hybrid perovskites: materials properties and emerging applications, MRS Commun. 5 (2015) 7–26, https://doi.org/10.1557/mrc.2015.6.

[24] P. Fan, D. Gu, G. Liang, J. Chen, J. Luo, Y. Xie, Z. Zheng, D. Zhang, Growth of high quality CH3NH3PbI3 thin films prepared by modified dual-source vapor evaporation, J. Mater. Sci. Mater. Electron. 27 (2016) 2321–2327, https://doi.org/10.1007/s10854-015-4028-6.

[25] H.S. Jung, N.-G. Park, Perovskite solar cells: from materials to devices, Small 11 (2015) 10–25, https://doi.org/10.1002/smll.201402767.

[26] N.G. Park, Perovskite solar cells: an emerging photovoltaic technology, Mater. Today 18 (2015) 65–72, https://doi.org/10.1016/j.mattod.2014.07.007.

[27] B. Cai, Y. Xing, Z. Yang, W.-H. Zhang, J. Qiu, High performance hybrid solar cells sensitized by organolead halide perovskites, Energy Environ. Sci. 6 (2013) 1480, https://doi.org/10.1039/c3ee40343b.

[28] M. Ganjian, M. Kolahdouz, A. Aletayeb, M. Norouzi, P. Ebrahimi, S. Pourjafari, M.S. Sanei Mousavi, ZnS shell-like CdS quantum dot-sensitized solar cell grown by SILAR approach; effect of electrolyte, counter electrode, and shell thickness, Vacuum (2016), https://doi.org/10.1016/j.vacuum.2017.02.007.

[29] F. Dehghan Nayeri, M. Kolahdouz, E. Asl-Soleimani, S. Mohajerzadeh, Low temperature carving of ZnO nanorods into nanotubes for dye-sensitized solar cell application, J. Alloys. Compd. 633 (2015), https://doi.org/10.1016/j.jallcom.2015.01.295.

[30] J.P. Mailoa, C.D. Bailie, E.C. Johlin, E.T. Hoke, A.J. Akey, W.H. Nguyen, M.D. McGehee, T. Buonassisi, A 2-terminal perovskite/silicon multijunction solar cell enabled by a silicon tunnel junction, Appl. Phys. Lett. 106 (2015) 121105, , https://doi.org/10.1063/1.4914179.

[31] B. Chen, M. Yang, S. Priya, K. Zhu, Origin of j – V hysteresis in perovskite solar cells, J. Phys. Chem. Lett. 7 (2016) 905–917, https://doi.org/10.1021/acs.jpclett.6b00215.

[32] M.I. Saidaminov, A.L. Abdelhady, B. Murali, E. Alarousu, V.M. Burlakov, W. Peng, I. Dursun, L. Wang, Y. He, G. MacUlan, A. Goriely, T. Wu, O.F. Mohammed, O.M. Bakr, High-quality bulk hybrid perovskite single crystals within minutes by inverse temperature crystallization, Nat. Commun. 6 (2015) 1–6, https://doi.org/10.1038/ncomms8586.

[33] S. Van Reenen, M. Kemerink, H.J. Snaith, Modeling anomalous hysteresis in perovskite solar cells, J. Phys. Chem. Lett. 6 (2015) 3808–3814, https://doi.org/10.1021/acs.jpclett.5b01645.

[34] J. Shi, J. Dong, S. Lv, Y. Xu, L. Zhu, J. Xiao, X. Xu, H. Wu, D. Li, Y. Luo, Q. Meng, Hole-conductor-free perovskite organic lead iodide heterojunction thin-film solar cells: high efficiency and junction property, Appl. Phys. Lett. 104 (2014) 063901, , https://doi.org/10.1063/1.4864638.

[35] F. Zhang, X. Yang, H. Wang, M. Cheng, J. Zhao, L. Sun, Structure engineering of hole–conductor free perovskite-based solar cells with low-temperature-processed

commercial carbon paste as cathode, ACS Appl. Mater. Interfaces 6 (2014) 16140–16146, https://doi.org/10.1021/am504175x.
[36] M. Masnadi-Shirazi, R.B. Lewis, V. Bahrami-Yekta, T. Tiedje, M. Chicoine, P. Servati, Bandgap and optical absorption edge of GaAs1 − xBix alloys with 0 < x < 17.8%, J. Appl. Phys. 116 (2014) 223506, https://doi.org/10.1063/1.4904081.
[37] P. Mandal, S. Sharma, Progress in plasmonic solar cell efficiency improvement: a status review, Renew. Sustain. Energy Rev. 65 (2016) 537–552, https://doi.org/10.1016/j.rser.2016.07.031.
[38] P. Kowalczewski, M. Liscidini, L.C. Andreani, Light trapping in thin-film solar cells with randomly rough and hybrid textures, Opt. Express 21 (2013) A808, https://doi.org/10.1364/OE.21.00A808.
[39] J.T. Black, R.A. Kohser, DeGarmo's Materials and Processes in Manufacturing Tenth Edition, 12th ed., John Wiley & Sons, 2017 (Accessed 23 March 2019), https://books.google.com/books?hl=en&lr=&id=JkkzDwAAQBAJ&oi=fnd&pg=PA1&dq=materials+and+processes+in+manufacturing&ots=GlIcyM_ozw&sig=BRKgNeLyRBkUGlXtXhRvRSZssXw.
[40] B.W. Schneider, N.N. Lal, S. Baker-Finch, T.P. White, Pyramidal surface textures for light trapping and antireflection in perovskite-on-silicon tandem solar cells, Opt. Express 22 (2014) A1422, , https://doi.org/10.1364/OE.22.0A1422.
[41] J. Lim, Y.S. Kwon, T. Park, Effect of coadsorbent properties on the photovoltaic performance of dye-sensitized solar cells, Chem. Commun. 47 (2011) 4147, https://doi.org/10.1039/c0cc04999a.
[42] J.-H. Im, I.-H. Jang, N. Pellet, M. Grätzel, N.-G. Park, Growth of CH3NH3PbI3 cuboids with controlled size for high-efficiency perovskite solar cells, Nat. Nanotechnol. 9 (2014) 927–932, https://doi.org/10.1038/nnano.2014.181.
[43] Q. Lin, A. Armin, R.C.R. Nagiri, P.L. Burn, P. Meredith, Electro-optics of perovskite solar cells, Nat. Photonics 9 (2015) 106–112, https://doi.org/10.1038/nphoton.2014.284.
[44] D. Shi, Y. Zeng, W. Shen, Perovskite/c-Si tandem solar cell with inverted nanopyramids: realizing high efficiency by controllable light trapping, Sci. Rep. 5 (2015) 16504, https://doi.org/10.1038/srep16504.